

A unified description of gravity- and kinematics-induced segregation forces in dense granular flows

Lu Jing¹, Julio M. Ottino^{1,2,3}, Richard M. Lueptow^{1,2,3†},
and Paul B. Umbanhowar²

¹Department of Chemical and Biological Engineering, Northwestern University, Evanston, IL 60208, USA

²Department of Mechanical Engineering, Northwestern University, Evanston, IL 60208, USA

³Northwestern Institute on Complex Systems (NICO), Northwestern University, Evanston, IL 60208, USA

(Received xx; revised xx; accepted xx)

Particle segregation is common in natural and industrial processes involving flowing granular materials. Complex, and seemingly contradictory, segregation phenomena have been observed for different boundary conditions and forcing. Using discrete element method simulations, we show that segregation of a single particle intruder can be described in a unified manner across different flow configurations. A scaling relation for the net segregation force is obtained by measuring forces on an intruder particle in controlled-velocity flows where gravity and flow kinematics are varied independently. The scaling law consists of two additive terms: a buoyancy-like gravity-induced pressure gradient term and a shear rate gradient term, both of which depend on the particle size ratio. The shear rate gradient term reflects a kinematics-driven mechanism whereby larger (smaller) intruders are pushed toward higher (lower) shear rate regions. The scaling is validated, without refitting, in wall-driven flows, inclined wall-driven flows, vertical silo flows, and free surface flows down inclines. Comparing the segregation force to the intruder weight results in predictions of the segregation direction that match experimental and computational results for various flow configurations.

1. Introduction

Flowing granular mixtures tend to segregate by size, density, or other physical properties. Understanding granular segregation is essential for industrial sectors where granular materials are mixed and de-mixed (Ottino & Khakhar 2000; Ottino & Lueptow 2008). Segregation also plays an important role in natural processes such as geophysical mass flows (Iverson 1997; Johnson *et al.* 2012) and bedload transport (Frey & Church 2009; Ferdowsi *et al.* 2017). Recent decades have seen rapid development in both physical interpretation and theoretical modeling of particle segregation, particularly in *dense* granular flows (Gray 2018; Umbanhowar *et al.* 2019). However, fundamental aspects of granular segregation at the particle level remain unclear.

Granular materials display a rich variety of segregation behaviors. In gravity-driven flows, small particles tend to percolate downward under gravity through interstices between large particles, displacing large particles upward. By contrast, systematic evidence of reverse segregation (i.e., large particles sink) has been reported depending on the size

† Email address for correspondence: r-lueptow@northwestern.edu

and density ratios of particle species, as well as the species concentration (Thomas 2000; Félix & Thomas 2004). In the absence of gravity (e.g., lateral segregation in vertical silo flows), large particles tend to migrate toward high shear rate regions (Fan & Hill 2011; Itoh & Hatano 2019), but the tendency reverses when the flow becomes dilute (Fan & Hill 2011). Although different mechanisms including geometric effects (Savage & Lun 1988), mass effects (Félix & Thomas 2004), and shear gradient dependence (Fan & Hill 2011) have been proposed, a unified picture remains elusive. As a result, current theoretical predictions rely on *ad hoc* assumptions or phenomenological closures (Gray & Thornton 2005; Marks *et al.* 2012; Hill & Tan 2014; Fan *et al.* 2014; Schlick *et al.* 2015; Larcher & Jenkins 2015; Tunuguntla *et al.* 2016; Chassagne *et al.* 2020).

The single intruder particle limit provides an avenue to investigate the physics of granular segregation. Previous studies using this approach focused on segregation kinematics (Tripathi & Khakhar 2011; van der Vaart *et al.* 2015; Jing *et al.* 2017) and forces (Tripathi & Khakhar 2011; Guillard *et al.* 2016; van der Vaart *et al.* 2018; Staron 2018; Kumar *et al.* 2019; Jing *et al.* 2020). Guillard *et al.* (2016) were the first to propose and use a virtual spring-based “force meter” in numerical simulations, which allows measurement of the segregation force on single intruder particles in sheared granular beds. In this approach, an intruder particle is tethered to a virtual spring that acts only in the segregation (z) direction (perpendicular to the shear flow in the x -direction). The spring applies a restoring force on the intruder that opposes segregation. This restoring force can be used to determine the segregation force F_{seg} , which, by definition, is nothing more than the net contact force in the z -direction on the intruder due to particle-particle interactions. It is therefore convenient, and unambiguous, to view segregation as a result of the imbalance between F_{seg} and other forces such as the gravitational force (if present). The central goal of this work is to characterize F_{seg} as a function of local flow conditions for various particle properties and system flow parameters, and validate this description across a wide range of different flow geometries.

Guillard *et al.* (2016) showed that, in two-dimensional (2D) confined flows, F_{seg} can be expressed as two additive terms that scale with the local pressure gradient ($\partial p/\partial z$) and the local shear stress gradient ($\partial\tau/\partial z$),

$$F_{seg}\Big|_{\text{confined flow}} = -\mathcal{A}(\mu, R)\frac{\partial p}{\partial z}V_i + \mathcal{B}(\mu, R)\frac{\partial\tau}{\partial z}V_i, \quad (1.1)$$

where $\mathcal{A}(\mu, R)$ and $\mathcal{B}(\mu, R)$ are dimensionless functions, $\mu = \tau/p$ is the local effective friction, R is the intruder-to-bed particle size ratio, and V_i is the intruder volume. Note that Guillard *et al.*'s original expression was applied to 2D disks and given in terms of the intruder “area” instead of volume. Note also that here “pressure” and “normal stress” are interchangeable ($p = \sigma_{zz}$) because small differences in normal stress components (σ_{xx} , σ_{yy} , σ_{zz}) are neglected, and $-\partial p/\partial z = \phi\rho g_z$ indicates (positive) hydrostatic pressure gradients, where ϕ is the bulk packing fraction, ρ is the material density of bed particles, and g_z is the z -component of the gravitational acceleration.

Expression (1.1) describes gravity- and shear-driven segregation in *confined*, wall-driven flows and has inspired follow-up studies including van der Vaart *et al.* (2018) and Jing *et al.* (2020) for different flow geometries. However, several important questions remain unexplored. First, although the two terms in (1.1) appear to separate normal- and shear-stress gradient contributions, the dependence of both pre-factors \mathcal{A} and \mathcal{B} on μ indicates that the two effects remain coupled, since μ depends on both p and τ , and, hence, their gradients. The influence of shear stress profiles seems to be unclear in other geometries as well. For example, in three-dimensional (3D) inclined chute flows, van der Vaart *et al.*

(2018) showed that the total segregation force is insensitive to shear stress gradients (which vary with the chute inclination), a finding we confirmed using a controlled-velocity approach that allows shear stress profiles to be specified (Jing *et al.* 2020). Second, while it is generally accepted that the pressure gradient-induced segregation force is related to “granular buoyancy” (Guillard *et al.* 2016; van der Vaart *et al.* 2018; Jing *et al.* 2020), the physical origin of the shear stress gradient contribution remains unexplained (Guillard *et al.* 2016). Third, as noted by Guillard *et al.* (2016), the scaling law described by (1.1) is based on 2D *confined* flows and does not predict the sinking of very large intruders observed in *free surface* flow experiments (Félix & Thomas 2004), which raises the question of how (1.1) applies to 3D unconfined flow configurations.

We recently developed a scaling law for F_{seg} that predicts whether an intruder rises or sinks in free surface flows (Jing *et al.* 2020), matching extensive experimental results across the broad size-density parameter space explored by Félix & Thomas (2004) and agreeing with inclined chute flow simulation results, including those of van der Vaart *et al.* (2018). The scaling law has a simple, buoyancy-like form:

$$F_{seg}\Big|_{\text{free surface flow}} \approx F_{seg}\Big|_{\text{“linear” flow}} = -f(R)\frac{\partial p}{\partial z}V_i, \quad (1.2)$$

where $f(R)$ is dimensionless and the flow velocity is “linear” (elaborated below). In contrast to $\mathcal{A}(\mu, R)$ and $\mathcal{B}(\mu, R)$ expressions in (1.1), $f(R)$ is insensitive to local flow properties (e.g., μ). This finding indicates that F_{seg} depends only on pressure gradients, but not shear stress gradients such as the second term of (1.1), in free surface flows that have an approximately linear velocity profile. Indeed, the buoyancy-like scaling of (1.2) on its own captures the chute flow results of van der Vaart *et al.* (2018), although they further decompose F_{seg} into separate lift- and buoyancy-like components.

The scaling law (1.2) is based on controlled-velocity flows where a stabilizing algorithm enforces a linear velocity profile (i.e., constant shear rate); gravity is also included to introduce inhomogeneous pressure and shear stress profiles (Jing *et al.* 2020). This linear-velocity flow represents an elementary flow where the segregation force can be easily connected with local flow properties, such as the shear rate, pressure, and stress gradients. A linear velocity profile is an accurate approximation for free surface flows at least over the extent of the profile in the vicinity of an intruder particle. However, for wall-driven flows where the velocity profile can be highly nonlinear, the local shear rate can vary significantly over a distance comparable to the intruder size (Fan & Hill 2011; Guillard *et al.* 2016). In these cases, higher-order effects may occur and the linear velocity assumption is not always appropriate.

To extend the applicability of the scaling (1.2) to more general situations where the velocity profile may be nonlinear, we propose in this paper that an additional contribution to the segregation force is associated with the local curvature of the velocity profile (i.e., the shear rate gradient $\partial\dot{\gamma}/\partial z$, where $\dot{\gamma} = \partial u/\partial z$ and u is the flow velocity in the streamwise x -direction). A unified form for F_{seg} is proposed:

$$F_{seg}\Big|_{\text{unified}} = -f^g(R)\frac{\partial p}{\partial z}V_i + f^k(R)\frac{p}{\dot{\gamma}}\frac{\partial\dot{\gamma}}{\partial z}V_i, \quad (1.3)$$

where the first term is identical to (1.2) and is gravity induced (hence $f^g(R)$); note that we only consider pressure gradients induced by gravity, although rotation or other body forces can also induce pressure gradients), while the second term represents a kinematics contribution (hence $f^k(R)$) that is related to the curvature of the velocity profile. Functional forms of $f^g(R)$ and $f^k(R)$ are established below as expressions (3.4)

and (3.5), respectively. It is important to note that, as demonstrated below, both $f^g(R)$ and $f^k(R)$ are independent of μ and the kinematics contribution is universal for all flow geometries that we consider, including confined and free surface flows, for a wide range of flow conditions from quasistatic to inertial. Interestingly, the kinematics description (1.3) and the stress description (1.1) are approximately equivalent if (and only if) the flow obeys a *local rheology* (Forterre & Pouliquen 2008), i.e., shear stresses depend only on local shear rates, leading to the μ dependence in (1.1); see Appendix A. However, this equivalence breaks down in flow regions that exhibit a *nonlocal rheology* (Kamrin 2019), thus limiting the generality of (1.1). Lastly, the specific form of the second term in (1.3) is inferred from a dimensional argument, and the relevance of all parameters (p , $\dot{\gamma}$, $\partial\dot{\gamma}/\partial z$, and V_i) is verified in this paper based on a comprehensive parametric study. In particular, while $f^g(R)$ is studied and established in our recent work (Jing *et al.* 2020), $f^k(R)$ is developed in this paper by extending the controlled-velocity flow from constant shear rate (Jing *et al.* 2020) to constant shear rate gradient (i.e., controlled curvature of the velocity profile), and varying the curvature extensively.

In §2 we introduce the simulation scheme that allows flow kinematics to be arbitrarily controlled, as well as other flow geometries that we use for validation. Then, the approach to measuring F_{seg} and model details are presented. In §3 we first focus on $R = 2$ and characterize the kinematics contribution to F_{seg} in the absence of gravity, after which we introduce gravity and show that the two terms in (1.3) are indeed additive. The proposed scaling law is then compared with results from other geometries, highlighting the universality of gravity- and kinematics-induced segregation forces. Finally, results for varying R are presented to establish the R dependence in scaling law (1.3). Conclusions are drawn in §4.

2. Methods

2.1. Flow configurations

We use the open-source discrete element method (DEM) code LIGGGHTS (Kloss *et al.* 2012) to simulate several different dense granular flows, which can be classified broadly into “confined” and “free surface” flows (figure 1). For confined flows, we vary the velocity profile with two different approaches: first, by directly controlling the velocity field (referred to as “controlled-velocity” flows; see below); second, by varying the direction of gravity in “wall-driven” flows. In each flow, a single intruder particle is placed in the middle of the flow depth to measure the segregation force F_{seg} (see figure 1i and §2.2). The focus is on how F_{seg} depends on the local curvature of the velocity profile.

As shown in figure 1, periodic boundaries are imposed in the streamwise (x) and spanwise (y) directions and the domain is sufficiently wide in both directions that, in steady state, gradients of the flow occur only in the normal (z) direction; that is, we only consider segregation in the z -direction. For controlled-velocity flows, gravity is always normal to the bottom wall, while for other flows, gravity may be tilted in the xz -plane to an angle of θ with respect to the z -axis. The gravity vector is denoted as $(g_x, 0, g_z) = (g \sin \theta, 0, -g \cos \theta)$, where g is the magnitude of the gravitational acceleration. To aid interpretation of the segregation direction, we use “up” and “down” (or similar terms) to refer to the positive and negative directions of the z -axis consistent with that in figure 1, even when gravity is turned off or is parallel to the flow (i.e., $g_z = 0$). The same convention applies to “top” and “bottom” walls. Bottom walls are always immobile, while top walls (absent in free surface flows) are reactive in the z -direction to maintain

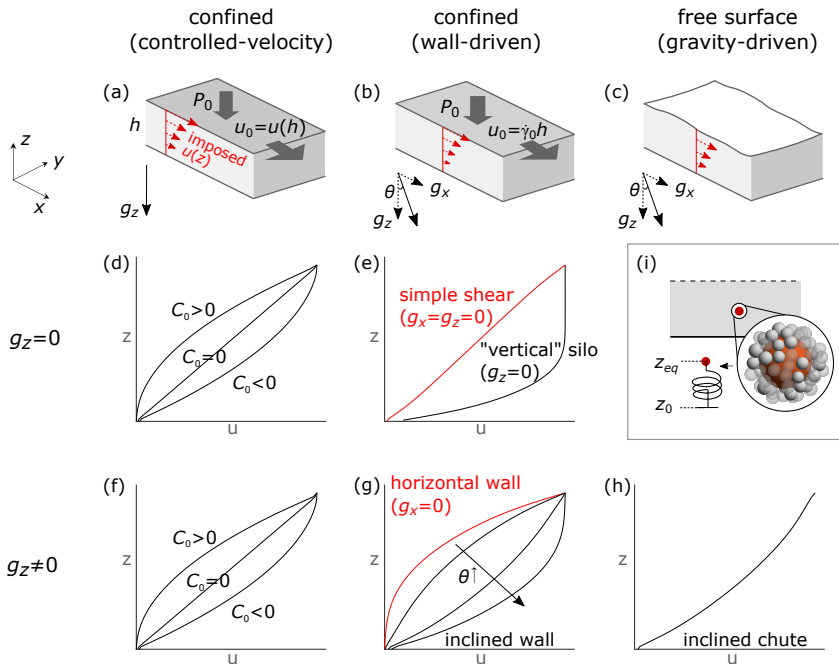


FIGURE 1. (a–h) Flow configurations and associated velocity profiles (see text for details). (i) Intruder particle (red) in the flow and tethered to a virtual vertical spring for segregation force measurement.

an overburden pressure P_0 and translate with velocity u_0 . All walls are roughened by randomly distributed stationary particles to reduce slippage (Jing *et al.* 2016).

In the following, each flow type is described with an emphasis on the curvature of its velocity profile and how the curvature is systematically varied.

2.1.1. Confined, controlled-velocity flows

Controlled-velocity flow, in which the flow velocity profile is specified, has been used previously to study granular rheology. While linear velocity profiles are usually imposed in the absence of gravity to achieve homogeneous shear (Lerner *et al.* 2012; Clark *et al.* 2018), it is also possible to impose arbitrary velocity profiles without gravity (Saitoh & Tighe 2019) or to add gravity for linear velocity profile flows (Fry *et al.* 2018; Duan *et al.* 2020*b*). Controlling the velocity profile allows us to vary shear rate gradients (i.e., curvatures of the velocity profile) independently of gravity, thereby isolating the gravity- and kinematics-related contributions to the segregation force.

To impose a particular streamwise velocity profile $u(z)$, a stabilizing force (in the x -direction) is applied to each particle at each DEM time step (Fry *et al.* 2018), including the intruder particle, and the top wall is translated at a matching speed $u(h)$, where h is the flow thickness. The stabilizing force applied on a particle is $A(u(z_p) - u_p)$, where z_p and u_p are the instantaneous particle position and velocity, respectively, and A is a constant. We use $A = 0.1 \text{ N} \cdot \text{s}/\text{m}$ in the controlled-velocity flows below, but increasing or decreasing A by an order of magnitude does not change the results significantly. Indeed, as detailed below, controlled-velocity flows follow the same granular rheology as homogeneous shear flow, indicating that particle-particle collisions dominate the particle rheology even when stabilizing forces are imposed.

To generate a constant shear rate gradient flow, we specify $u(z)$ as

$$u(z) = (\dot{\gamma}_0 - \frac{C_0 h}{2})z + \frac{C_0}{2}z^2, \quad (2.1)$$

where $\dot{\gamma}_0$ and C_0 are, respectively, a characteristic shear rate and the controlled curvature (i.e., shear rate gradient). For this profile, we have

$$\dot{\gamma}(z) = \dot{\gamma}_0 - \frac{C_0 h}{2} + C_0 z, \quad (2.2)$$

and

$$\frac{\partial \dot{\gamma}}{\partial z} = C_0. \quad (2.3)$$

The specific form of (2.1) is chosen for several reasons. First, the local shear rate in the middle of the flow (where the intruder is placed) is $\dot{\gamma}(h/2) = \dot{\gamma}_0$ independent of C_0 . Second, the shear rate gradient in the simulation is homogeneous (except within a few bed particle diameters of the upper and lower boundaries; see figure 2 below) based on (2.3); by varying C_0 from negative to positive, the concavity and local curvatures of the velocity profile around the intruder are systematically varied and precisely controlled (figures 1d and f). Third, the velocity at the upper boundary, $z = h$, is $u_0 = \dot{\gamma}_0 h$, which is consistent with the top wall velocity in wall-driven flows (figure 1b). Furthermore, we constrain gravity so that it is always in the z -direction; that is, $g_x = 0$. Other forms of $u(z)$, such as power-law and exponential functions, could be used in place of (2.1), but these do not have the advantage of a constant $\partial \dot{\gamma} / \partial z$ throughout the flow domain. Nevertheless, we have verified that these alternative velocity profiles produce segregation forces that are consistent with the scaling (1.3).

Apart from systematically varying the shear rate gradient C_0 , we also vary P_0 , $\dot{\gamma}_0$, and g_z to explore their effects on the segregation force on a single intruder particle. A key advantage of the controlled-velocity geometry is that the imposed velocity profile is unaffected by gravity; the flow adjusts its shear stress profiles in response to changed gravitational fields while maintaining the same flow kinematics. As shown schematically in figures 1d and f, identical velocity profiles are achieved for the $g_z = 0$ and $g_z \neq 0$ cases while keeping other system parameters constant.

2.1.2. Wall-driven flows

In wall-driven flows, overburden pressure P_0 and velocity $u_0 = \dot{\gamma}_0 h$ are imposed at the top wall to drive the flow without directly controlling the velocity profile (note that in wall-driven flows we use $\dot{\gamma}_0$ to characterize the top wall velocity, consistent with the notation for controlled-velocity flows). The concavity of the velocity profile of wall-driven flows is altered by varying the direction of gravity (figures 1e and g). With no gravity ($g_x = g_z = 0$), the flow is simple shear with a nearly linear velocity profile (figure 1e), and segregation does not occur because both the pressure gradient and shear rate gradient are zero.

When gravity is parallel to the flow direction ($\theta = 90^\circ$, $g_x \neq 0$, $g_z = 0$), shear stress gradients develop along the z -direction and the velocity profile is concave up (negative $\partial \dot{\gamma} / \partial z$), as shown in figure 1(e). Shear is localized near the bottom wall, above which is a plug-flow zone. This flow is similar to half of a “vertical” silo flow (GDR MiDi 2004), albeit horizontally placed in our coordinate system. Segregation in the z -direction is driven only by shear as there is no pressure gradient ($g_z = 0$).

When gravity is perpendicular to the flow ($\theta = 0$, $g_x = 0$, $g_z \neq 0$), a flowing

layer develops near the top wall with concave-down (positive $\partial\dot{\gamma}/\partial z$) velocity profiles (figure 1g). Shear stress is homogeneous in this geometry, because the only external forcing in the x -direction is applied from the top wall (Guillard *et al.* 2016). However, both the pressure gradient due to gravity and the non-linear velocity profile (or, the shear rate gradient) are expected to contribute to segregation.

As θ increases from 0 toward 90° ($\theta > 0$, $g_x \neq 0$, $g_z \neq 0$; “inclined wall-driven” flows in figure 1g), the velocity profile changes from concave down to concave up, and the kinematics- and gravity-related segregation mechanisms can either compete or cooperate.

2.1.3. Free surface, gravity-driven flows

Common free surface flows include chute flow, heap flow, and surface flow in rotating tumblers. Here we study relatively thick flows (about 40 particles deep) down an inclined streamwise and spanwise periodic chute that exhibit Bagnold-like, concave-up velocity profiles (figure 1h). Thin chute flows (Silbert *et al.* 2003; Louge 2003; Weinhart *et al.* 2012; Kamrin & Henann 2015) or shallow flowing layers in heap and rotating-drum flows (GDR MiDi 2004; Kamrin & Koval 2012) will be addressed in separate work as these flows are likely to be strongly affected by bottom or sidewall boundaries.

2.2. Segregation force measurement

We measure the segregation force on a single intruder particle in each flow simulation following the approach of Guillard *et al.* (2016). The intruder is tethered to a virtual spring that senses forces only in the z -direction, which allows the intruder to deviate from the initial height z_0 and fluctuate around an equilibrium position z_{eq} (figure 1i). In equilibrium, F_{seg} , the net contact force on the intruder perpendicular to the flow (in the z -direction), is balanced by the spring force and the intruder weight, i.e., $F_{seg} = k(z_{eq} - z_0) + m_i g_z$, where k is the spring stiffness and m_i is the intruder mass. Note that F_{seg} represents the *mean* segregation force, even though the random action of contacting particles fluctuates in time. The uncertainty in F_{seg} (error bars) is estimated based on temporally correlated fluctuations of the intruder position around z_{eq} (Zhang 2006). The measurement of F_{seg} is insensitive to k for 3D configurations (van der Vaart *et al.* 2018) as the intruder is free to explore the xy -plane. We use stiff springs (typically, $k = 100$ N/m) to ensure that z_{eq} is close to z_0 such that local flow conditions around the intruder can be a priori controlled (or estimated in flows without directly controlled velocity profiles).

2.3. Model parameters and flow conditions

The flow domain in all simulations is $30d$ long (x), $20d$ to $30d$ wide (y), and $40d$ deep (z) (adjusted to avoid boundary effects), and contains bed particles of diameter d and density ρ . A single intruder particle of size ratio $R = d_i/d$ and density ratio $R_\rho = \rho_i/\rho$, where d_i and ρ_i are the intruder diameter and density, is placed in the middle of the flow. In previous work we varied both R and R_ρ to study forces driving combined size and density segregation (Jing *et al.* 2020). Here, to simplify the parameter space, we only report results for $d = 5$ mm (with 10% size polydispersity), $\rho = 2500$ kg/m³, $R_\rho = 1$, and $0.2 \leq R \leq 8$. However, varying d , ρ , or R_ρ does not change the scaling of F_{seg} . Particle interactions are calculated using the Hertz contact model with Young’s modulus 5×10^7 Pa, Poisson’s ratio 0.4, restitution coefficient 0.8, and friction coefficient 0.5; varying these parameters has negligible influence on the results, except for friction $\lesssim 0.3$ (see Supplemental Material for Jing *et al.* (2020)).

System parameters are varied for each flow geometry (figure 1) to achieve a wide range of local flow conditions (e.g., $\partial p/\partial z$, $\partial\dot{\gamma}/\partial z$, p , $\dot{\gamma}$) around the intruder, which are then

associated with F_{seg} according to the proposed relation (1.3). Local flow conditions are estimated for each simulation at $z = z_{eq}$ based on spatially and temporally averaged flow fields along the z -direction. Steady-state flow and stress profiles are estimated based on $1d$ -thick bins along the flow depth (z) that span the simulation domain in the xy -plane. For a given instant at steady state, we first compute averaged velocity and contact stresses (Silbert *et al.* 2001) in each bin based on particles centered in that bin, including the intruder particle, and then smooth the depth-wise profile spatially using a moving average filter (typically spanning five equally weighted bins). The profiles are then averaged in time, typically using 200 snapshots for steady state conditions. First or second-order gradients of the velocity and stress profiles (e.g., $\dot{\gamma}$, $\partial\dot{\gamma}/\partial z$, $\partial p/\partial z$) are calculated using central differences. Although an intruder particle can change local flow structures in its vicinity (van der Vaart *et al.* 2018; Jing *et al.* 2020), we have verified that local disturbances due to the presence of the intruder are smoothed out (see smoothed flow profiles in figures 2, 4, and 7 below) and that details of the averaging method do not affect the results.

The flow at $z = z_{eq}$ is characterized by the local inertial number $I(z_{eq}) = \dot{\gamma}(z_{eq})d\sqrt{\rho/p(z_{eq})}$, which is varied broadly from 0.004 to 0.44 with $500 \leq P_0 \leq 2500$ Pa and $10 \leq \dot{\gamma}_0 \leq 40$ s⁻¹ for controlled-velocity and confined flows or $22^\circ \leq \theta \leq 28^\circ$ for inclined chute flows; varying g also influences $I(z_{eq})$. For brevity, we mainly report $I(z_{eq})$ (simply referred to as I below) instead of system parameters when identifying flow characteristics; detailed simulation parameters (both controlled system parameters and measured local parameters) are provided as supplementary material.

3. Results and discussion

3.1. Segregation forces for $R = 2$

Focusing first on size ratio $R = 2$ and density ratio $R_\rho = 1$, we vary local curvatures in controlled-velocity flows following (2.1) in the absence of gravity ($g_z = 0$) to study the kinematics-dependent part of F_{seg} , and then add gravity ($g_z > 0$) to study the gravity-dependent part. Results from other flow geometries are used to validate the scaling.

3.1.1. Kinematics contribution (no gravity)

Figure 2 shows data from a representative set of controlled-velocity simulations with varying C_0 but fixed P_0 and $\dot{\gamma}_0$ (thus fixed I around the intruder); $\dot{\gamma}_0$, P_0 , and h are used for normalization. In figure 2(a), as C_0 is varied from negative (darker curves) to positive (lighter curves), the velocity profile varies from concave up to concave down, including a linear case with no curvature ($C_0 = 0$). A symbol marks the intruder position z_{eq} on each curve, which is always midway between the upper and lower walls to minimize wall effects. Figure 2(b) shows that, although the shear rate profile varies with C_0 , the local shear rate at the position of the intruder ($z/h \approx 0.5$) is always $\dot{\gamma}_0$ due to the imposed velocity profile (2.1). Figure 2(c) shows that the imposed velocity profile results in a constant local shear rate gradient $\partial\dot{\gamma}/\partial z$ across nearly the entire flow domain (except at the upper and lower walls) with dimensionless curvatures $C_0h/\dot{\gamma}_0$ varying from -2 to 2 . Since $g_z = 0$, pressure is uniform across the flow domain ($p(z)/P_0 \approx 1$), as shown in figure 2(d). However, the shear stress in figure 2(e) varies somewhat with depth due to the imposed velocity profiles, although its value at the location of the intruder is identical for all cases.

The key measurement here, the dimensionless force F_{seg}/P_0h exerted by bed particles on the intruder based on the measured virtual spring force, is plotted in figure 2(f)

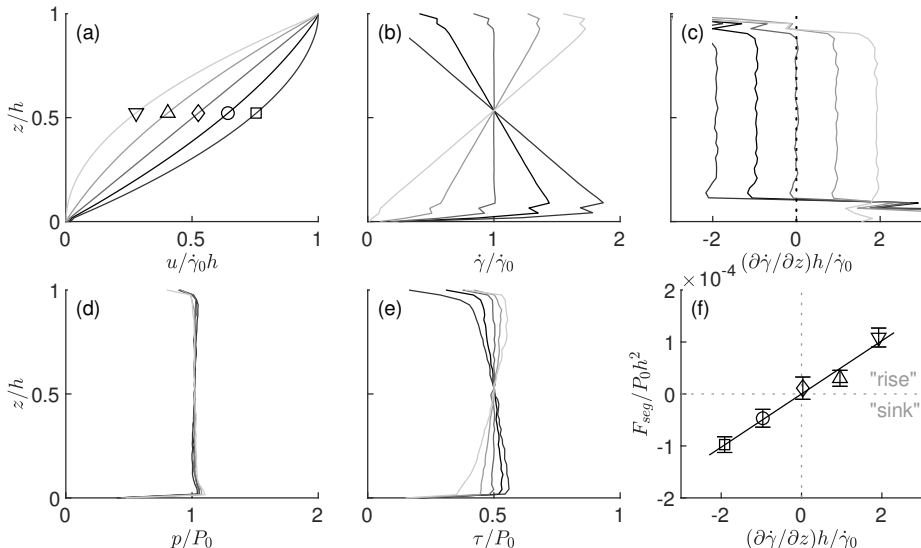


FIGURE 2. Typical results for controlled-shear-rate-gradient flows ($g_z = 0$, $P_0 = 1000$ Pa, $\dot{\gamma}_0 = 30$ s $^{-1}$). (a–e) Profiles of the normalized velocity, shear rate gradient, pressure, and shear stress, respectively. Darker to lighter colors indicate C_0 varying from negative to positive ($-2 \leq C_0 h / \dot{\gamma}_0 \leq 2$). Symbols in (a) indicate the steady-state z -location of the intruder. (f) Measured dimensionless segregation force $F_{seg}/P_0 h^2$ vs. dimensionless shear rate gradient $(\partial\dot{\gamma}/\partial z)h/\dot{\gamma}_0$. Symbols correspond to those in (a), and the solid line indicates a linear fit to the data through the origin. Error bars represent the uncertainty of F_{seg} due to its fluctuations in time (see §2.2).

against the dimensionless local curvature $(\partial\dot{\gamma}/\partial z)h/\dot{\gamma}_0$. It is evident that a non-linear flow velocity profile alone induces a net contact force on the intruder that drives segregation. Since F_{seg} is the only (net) force acting on the intruder in the no-gravity situation, negative values of F_{seg} correspond to the large intruder “sinking” (in the coordinate system of figure 1) toward high-shear regions, consistent with the trend of shear-driven segregation in *dense* vertical silo flows (Fan & Hill 2011). Similarly, positive values of F_{seg} indicate the large intruder “rising,” again, toward high-shear regions (see “rise” and “sink” in figure 2f). The relationship between F_{seg} and $\partial\dot{\gamma}/\partial z$ is linear and through the origin, indicating no segregation force when there is no shear rate gradient, as would be expected. Note that both negative and positive curvatures are considered here despite the apparent symmetry of the segregation behavior because the flow system we use is slightly asymmetric; the bottom wall is fixed whereas the top wall moves slightly in the z -direction in response to the constant P_0 boundary condition.

To explore the effect of local flow conditions on F_{seg} , we repeat the cases in figure 2 with nine different combinations of P_0 and $\dot{\gamma}_0$ (in total 59 simulations), leading to local inertial numbers I varying from 0.05 to 0.44 (see figure 3b inset for $\mu(I)$ data). As shown in figure 3(a), the dependence of F_{seg} on $\partial\dot{\gamma}/\partial z$ varies with I when presented in physical units; the slope of the linear correlation tends to decrease as I increases (from blue to red symbols). Note that since data have more scatter for small I approaching the quasistatic limit (< 0.1), a finer variation of $\partial\dot{\gamma}/\partial z$ is used in these cases resulting in more data points for small I .

To collapse the data, we consider the rescaled curvature from (1.3), $(p/\dot{\gamma})(\partial\dot{\gamma}/\partial z)V_i$, in units of force, which results in excellent collapse for the full range of I that we examine, as shown in figure 3(b); that is,

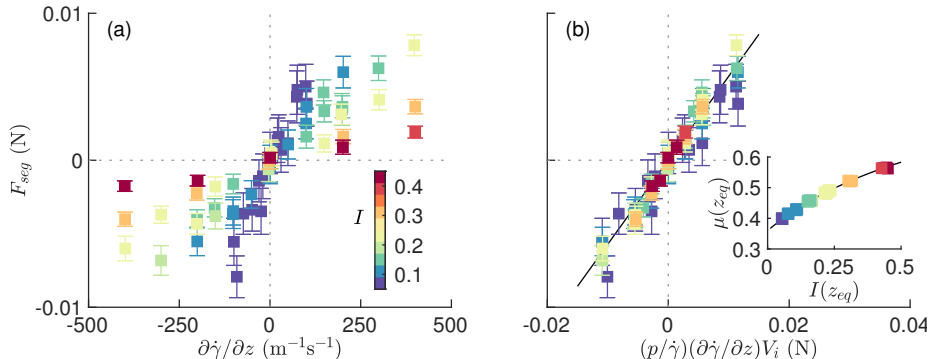


FIGURE 3. Influence of P_0 and $\dot{\gamma}_0$ on F_{seg} in controlled-velocity flows ($g_z = 0$). A range of local inertial numbers, $0.05 \leq I \leq 0.44$ (color bar), is explored with $500 \text{ Pa} \leq P_0 \leq 2000 \text{ Pa}$ and $10 \text{ s}^{-1} \leq \dot{\gamma}_0 \leq 40 \text{ s}^{-1}$; for each $(P_0, \dot{\gamma}_0)$ combination, $C_0 h/\dot{\gamma}_0$ is varied from -2 to 2 to generate negative to positive curvatures $\partial\dot{\gamma}/\partial z$. (a) Non-collapse of F_{seg} vs. $\partial\dot{\gamma}/\partial z$. (b) Collapse of F_{seg} vs. $(p/\dot{\gamma})(\partial\dot{\gamma}/\partial z)V_i$. The solid line is a linear fit through $(0, 0)$ with slope 0.57 . Inset: Local $\mu(I)$ measurements at $z = z_{eq}$. Reference curve $\mu(I) = 0.36 + (0.94 - 0.36)/(0.8/I + 1)$ is obtained using our simple shear data far from boundaries and with no intruder.

$$F_{seg}^k := F_{seg} \Big|_{g_z=0} \propto \frac{p}{\dot{\gamma}} \frac{\partial\dot{\gamma}}{\partial z} V_i, \quad (3.1)$$

where F_{seg}^k denotes the kinematics-induced part of F_{seg} . The proportionality constant is 0.57 based on the linear fit in figure 3(b), and the correlation passes through the origin, indicating that no other effects are present.

The force scaling in (3.1) is based on dimensional analysis. Indeed, when $g_z = 0$, natural choices for normalizing F_{seg}^k and $\partial\dot{\gamma}/\partial z$ are pd_i^2 and $\dot{\gamma}/d_i$, respectively, and the resulting scaling, $F_{seg}^k/pd_i^2 \propto (\partial\dot{\gamma}/\partial z)d_i/\dot{\gamma}$, or $F_{seg}^k \propto (p/\dot{\gamma})(\partial\dot{\gamma}/\partial z)d_i^3$, is equivalent to (3.1). However, here we prefer the volume-based expression (3.1) for consistency with the buoyancy-like term in (1.3) and following the previous scaling law (1.1). Moreover, the scaling $F_{seg}^k/pd_i^2 \propto (\partial\dot{\gamma}/\partial z)d_i/\dot{\gamma}$ is similar to the normalization in figure 2f except that the system length scale h is replaced by the intruder diameter d_i (giving rise to V_i) and that local flow conditions are used. To confirm that d_i is the relevant length scale, we verified (omitted for brevity) that varying the flow thickness h does not change the scaling of F_{seg}^k , but doubling both d and d_i (with fixed $R = 2$) leads to a segregation force eight times larger, as the scaling predicts.

The curvature-based scaling (3.1) indicates that the shear rate gradient drives segregation in the absence of gravity. Although it is also possible to express a force scale in other ways, such as one related to the shear stress gradient or the granular temperature gradient (note that no pressure gradient is present so far), we have verified that the current form (3.1) results in the simplest scaling while other choices do not collapse the data as well as the scaling used here. For instance, using $\partial\tau/\partial z$ leads to scaling factors that depend on I (or μ), similar to those reported in Guillard *et al.* (2016), which not only complicates the function but also reduces the generality of the scaling because $\mu(I)$ is not necessarily unique across flow geometries or in regions where nonlocal effects occur (GDR MiDi 2004); see also §3.1.3. Nevertheless, in Appendix A we demonstrate that if the flow obeys a local rheology (e.g., $\mu(I)$), our $\partial\dot{\gamma}/\partial z$ -based scaling is equivalent to the $\partial\tau/\partial z$ -based scaling proposed by Guillard *et al.* (2016).

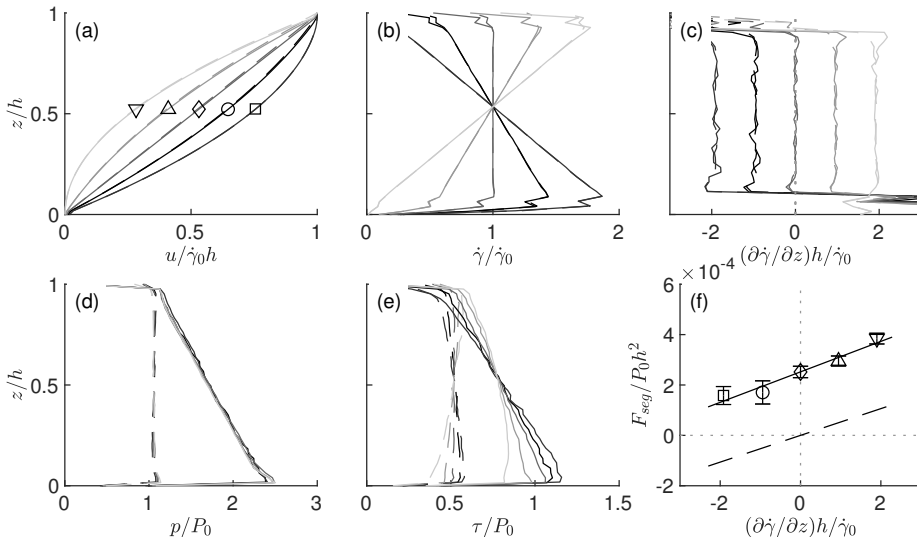


FIGURE 4. Same as figure 2 except with additional data for $g_z = 5 \text{ m/s}^2$ (solid curves). Dashed curves are the $g_z = 0$ data in figure 2.

3.1.2. Adding gravity

With gravity ($g_z > 0$), F_{seg} changes due to the induced pressure gradient. Figure 4 shows the same set of controlled-velocity flows as in figure 2 except with $g_z = 5 \text{ m/s}^2$. The kinematics profiles (solid curves in figures 4a–c) are nearly identical to their no-gravity counterparts (dashed curves) because velocity profiles are imposed. Stress profiles, on the other hand, change significantly in response to the added gravitational field (while granular rheology remains the same; see below). Both pressure and shear stress fields in figures 4(d) and (e) now include a hydrostatic component that is proportional to $\phi\rho g_z$. With these changes in the stress fields, F_{seg} remains proportional to the rescaled curvature (symbols and solid line in figure 4f), but with a substantial positive offset compared to the no-gravity results (dashed line in figure 4f); the slopes of the two lines are nearly identical, indicating that the gravity-induced contribution to F_{seg} does not change the kinematics contribution. Thus, the two terms in (1.3) are additive.

Next we consider a broader range of cases than in figure 4 by varying P_0 and $\dot{\gamma}_0$ as well as g_z (75 simulations in total). Figure 5(a) shows that the data for F_{seg} at different values of P_0 and $\dot{\gamma}_0$, when plotted against $(p/\dot{\gamma})(\partial\dot{\gamma}/\partial z)V_i$, collapse onto lines corresponding to each non-zero value of g_z (similar to Figure 3b for $g_z = 0$). As g_z is increased from 0 (dashed line), the dependence of F_{seg} on $p/\dot{\gamma}(\partial\dot{\gamma}/\partial z)V_i$ remains linear (solid lines) with a slope independent of g_z but shifted upward due to the imposed gravity. This further confirms the conclusion from figure 4(f) that the two terms in (1.3) are additive. Furthermore, F_{seg} remains insensitive to I (indicated by the symbol colors) over the range examined ($0.05 < I < 0.35$; note that varying g_z tends to affect the range of I), and the rheological data of controlled-velocity flows (when gravity is turned on) still follow the $\mu(I)$ curve for simple shear (figure 5b inset).

Because the gravity- and kinematics-related terms are additive, it is possible to use (3.1) to characterize the gravity-induced portion of the segregation force by simply subtracting F_{seg}^k from F_{seg} , which is plotted against $-(\partial p/\partial z)V_i$ in figure 5(b). All data collapse onto a line passing through the origin, which indicates a buoyancy-like scaling consistent with the one we proposed (Jing *et al.* 2020) based only on constant-

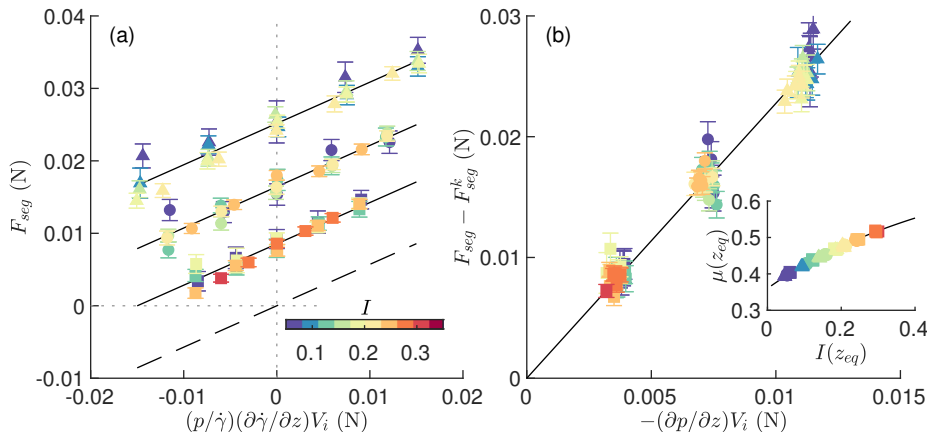


FIGURE 5. (a) Measured segregation force in controlled-velocity flows with $g_z = \{5, 9.81, 15\}$ m/s². For each g_z , a range of local inertial numbers (color bar) and local curvatures (horizontal axis) are explored with $500 \text{ Pa} \leq P_0 \leq 1500 \text{ Pa}$, $10 \text{ s}^{-1} \leq \dot{\gamma}_0 \leq 40 \text{ s}^{-1}$ and $-2 \leq C_0 h / \dot{\gamma}_0 \leq 2$. Solid lines are linear fits for the same g_z (g_z increases from bottom to top), while the dashed line represents $g_z = 0$ results; all lines have the same slope of 0.57. (b) $F_{seg} - F_{seg}^k$ vs. $-(\partial p / \partial z) V_i$. The solid line is a linear fit with slope 2.28 that extends through the origin. Inset: Local $\mu(I)$ measurements at $z = z_{eq}$, compared to simple shear results (curve; see figure 3 caption).

shear-rate flows (i.e., $F_{seg}^k = 0$). That the fit passes through the origin indicates that F_{seg} is completely described by the additive combination of gravitational and kinematic contributions, as indicated by (1.3). Note that the quadratic controlled-velocity profiles (2.1) reduce to linear-velocity profiles for $C_0 = 0$, and using only $C_0 = 0$ data produces the same linear fit as that in figure 5(b) (not shown as they are virtually identical). This again supports the assumption in (1.3) that the gravity- and kinematics-induced segregation forces are additive, and indicates that the gravity-related part can be measured using linear controlled-velocity flows, as in Jing *et al.* (2020). Specifically,

$$F_{seg}^g := F_{seg} \Big|_{\partial \dot{\gamma} / \partial z = 0} \propto -\frac{\partial p}{\partial z} V_i, \quad (3.2)$$

where the proportionality constant is 2.28 according to figure 5(b).

3.1.3. Validation in other flow geometries

In the previous two sections we establish scaling laws for the gravity- and kinematics-induced segregation forces that determine the net segregation force (for $R = 2$),

$$F_{seg} = F_{seg}^g + F_{seg}^k = -f^g \frac{\partial p}{\partial z} V_i + f^k \frac{p}{\dot{\gamma}} \frac{\partial \dot{\gamma}}{\partial z} V_i, \quad (3.3)$$

with $f^k = 0.57$ and $f^g = 2.28$ based on controlled-velocity results for a wide range of inertial numbers ($0.05 < I < 0.35$). The two terms depend on several local flow properties, including $\partial p / \partial z$, $\partial \dot{\gamma} / \partial z$, p , and $\dot{\gamma}$, but the relative magnitude of the two terms can vary significantly for different flow geometries. Hence, we now show that (3.3) remains valid in other geometries, including confined and free surface flows, while keeping $R = 2$.

Following the naming convention in figure 1, we measure F_{seg} in vertical silo (confined, $g_z = 0$), horizontal wall-driven (confined, $g_x = 0$), inclined wall-driven (confined, $g_x \neq 0$, $g_z \neq 0$), and inclined chute flows (free surface), each with broadly varied system parameters covering a wide range of inertial numbers, shear rate gradients (curvatures),

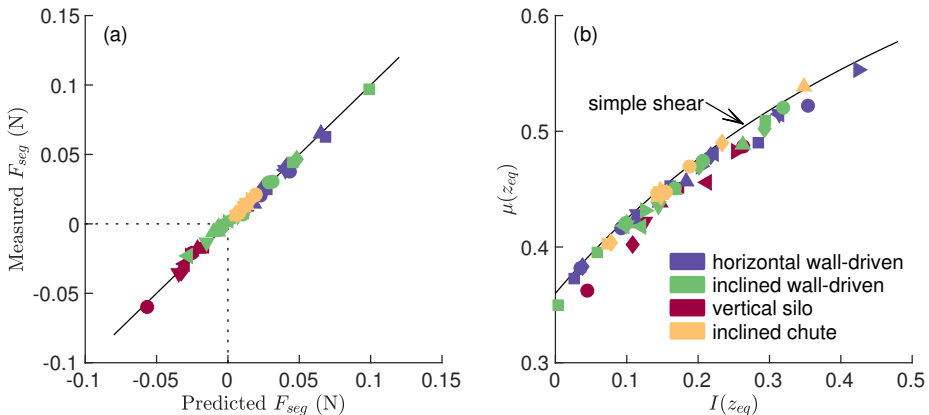


FIGURE 6. (a) Comparison of predicted F_{seg} (3.3) and measured F_{seg} in four flow geometries, each with widely varied system parameters (see §2.3 for the range of parameters). The line corresponds to a perfect match between predicted and measured values. (b) Measured $\mu(I)$ from simulations at $z = z_{eq}$ compared to reference curve from simple shear simulations (see figure 3 caption).

and pressure gradients (for $g_z \neq 0$) for $R = 2$. Results from 52 simulations across all flow geometries are reported in figure 6(a), in which the values for F_{seg} measured in the simulations are plotted against predictions of (3.3). The agreement between the measured values and the predictions is remarkable, especially given the broad range of flow geometries and flow conditions that are considered. The broad range of flow conditions is further amplified in figure 6(b), where local rheological data for the cases are presented, ranging from quasistatic ($I < 0.1$) to inertial flow regimes.

Three key points of figure 6 merit elaboration before the results are discussed in greater detail. First, the scaling (3.3) used to predict F_{seg} has only two independently determined parameters (f^k and f^g), yet its predictions are accurate across flow geometries with widely varying boundary conditions and forcing. Second, vertical silo results of F_{seg} in figure 6(a) are always negative due to the negative curvatures of the velocity profile (figure 1e), whereas horizontal wall-driven results of F_{seg} are positive due to the added effect of positive curvatures (figure 1g) and gravity-induced contributions. For inclined wall-driven flows, F_{seg} is either positive or negative due to the net effect of the flow velocity curvature (depending on θ) and gravity. Inclined chute flow results in figure 6(a) are always positive and span a much narrower range; in fact, as illustrated below, F_{seg}^k is nearly negligible in free surface flows compared to F_{seg}^g . Third, rheological data in figure 6(b) for different flow geometries deviate slightly from the simple shear rheology, yet this deviation does not affect the accurate prediction of F_{seg} in figure 6(a). Specifically, compared to the reference curve for simple shear, the confined flows without a controlled-velocity profile show systematic deviations that can be attributed to nonlocal effects near the edge of a localized shear layer (Kamrin & Koval 2012). In contrast, inclined chute flows and controlled-velocity flows (see insets in figures 3 and 5) closely follow the $\mu(I)$ curve for simple shear. Nevertheless, the prediction made by (3.3) remains accurate despite these variations in rheology, which stands in contrast to shear stress gradient based scaling (1.1) that is μ dependent (Guillard *et al.* 2016).

To better illustrate how gravity and flow kinematics contribute to the net segregation force in different flow geometries, we select representative cases for each geometry and present their velocity profiles, rheological data, and the two components of F_{seg} in fig-

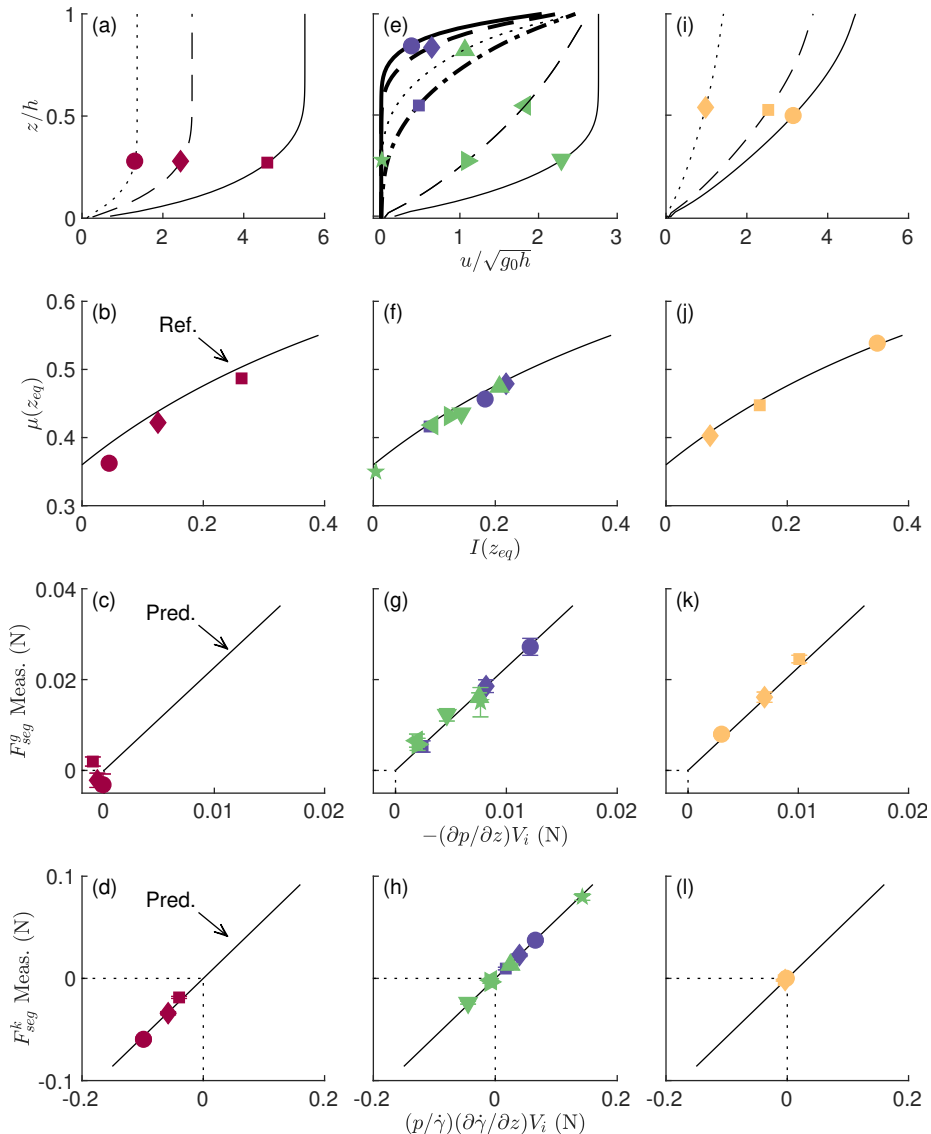


FIGURE 7. Representative results from vertical silo flows (left), horizontal and inclined wall-driven flows (middle), and inclined chute flows (right); color schemes match those in figure 6. Curves in the second row are reference $\mu(I)$ curves based on simple shear results. The predicted lines in the last two rows have slopes of 2.28 and 0.57, respectively, based on (3.3).

ure 7. A length scale h and a velocity scale $\sqrt{g_0 h}$ are consistently used for normalization, where $g_0 = 9.81 \text{ m/s}^2$ is fixed even though g is case specific.

Vertical silo flows. Figure 7(a) shows velocity profiles (curves) and steady-state locations of the intruder (symbols) for three (out of a total of eight) representative vertical silo simulations (with varying u_0 but the same P_0 and g_x). In vertical silo flows, shear is localized near the bottom wall with a concave-up velocity profile (negative curvature) connected to a plug-flow zone. The intruder is placed in the shear zone ($z_{eq}/h \approx 0.25$). Figure 7(b) shows rheological measurements around the intruder (symbols), which deviate from the simple shear reference curve (solid line) due to nonlocal effects in

localized shear. The small deviation of the rheological data in this flow geometry is robust (e.g., increasing particle stiffness by a factor of ten does not change the result significantly); nevertheless, the scaling of F_{seg} is unaffected by this variation in rheology.

Figures 7(c) and (d) show scaling of gravity- and kinematics-components of F_{seg} in the vertical silo flow simulations. To obtain *measured* F_{seg}^g and F_{seg}^k (vertical axes), we subtract $0.57(p/\dot{\gamma})(\partial\dot{\gamma}/\partial z)V_i$ and $-2.28(\partial p/\partial z)V_i$ from the total measured F_{seg} , respectively, using local flow properties. The measured F_{seg}^g and F_{seg}^k are then compared to force scales $-(\partial p/\partial z)V_i$ and $(p/\dot{\gamma})(\partial\dot{\gamma}/\partial z)V_i$, showing excellent agreement with the predicted solid lines in figures 7(c) and (d). More specifically, data in figure 7(c) cluster around (0,0) because $g_z = 0$, whereas data in figure 7(d) spread along the negative portion of the predicted line because of differing negative curvatures. Therefore, the net effect of the total F_{seg} for vertical silo flows is negative, meaning that an intruder tends to be pushed toward the immobile wall (high shear rate regions), agreeing with previous *dense* silo flow simulations (Fan & Hill 2011).

Horizontal wall-driven flows. Thick curves in figure 7(e) are velocity profiles of selected horizontal wall-driven flows (three of 16 simulations for this condition) that are concave down (positive curvature) in the shear zone close to the top moving wall. The selected cases differ only in g_z but have the same u_0 and P_0 ; the intruder fluctuates either around $z_{eq}/h \approx 0.75$ or $z_{eq}/h \approx 0.5$ (blue symbols). Figure 7(f) shows that the rheological measurements for wall-driven flows deviate only slightly from the simple shear reference curve. This, again, does not affect the scaling of the two components of F_{seg} , which follow the predictions in both figures 7(g) and (h). Results of F_{seg}^k for these positive-curvature velocity profiles fall along the positive portion of the predicted line in figure 7(g), adding to F_{seg}^g , which is also positive. This indicates that the intruder tends to be pushed upward by the net F_{seg} in wall-driven flows; imbalances between F_{seg} and the intruder weight ($m_i g_z$) determine whether the intruder rises or sinks (Jing *et al.* 2020).

Inclined wall-driven flows. Thin curves in figure 7(e) are velocity profiles of inclined wall-driven flows that transition from concave down (dotted) to concave up (dashed and solid) for $\theta = \{10, 30, 45\}^\circ$. The rheology (figure 7f) and F_{seg}^g (green symbols in figure 7g) results are similar to normal wall-driven flows ($\theta = 0$), but F_{seg}^k (figure 7h) for inclined wall-driven flows varies from negative to positive due to the changed sign of $\partial\dot{\gamma}/\partial z$. Results match predictions (figures 7g and h) even when intruders are repositioned at different locations from $z_{eq}/h \approx 0.25$ to $z_{eq}/h \approx 0.75$, resulting in a wide range of local inertial numbers including a quasistatic case near the bottom of the flow (star symbol on the thin dotted curve in figure 7e).

Inclined chute flows. Finally, results of selected free-surface, inclined chute flows with $\theta = \{22, 24, 28\}^\circ$ and corresponding $g = \{5, 9.81, 15\}$ m/s² are presented in figures 7(i–l), covering a wide range of inertial numbers and pressure gradients. The Bagnold-type velocity profiles are always concave up (figure 7i), and local rheological measurements match the simple shear reference curve (figure 7j). Interestingly, as shown in figure 7(l), the rescaled local curvatures are always nearly zero even though the shear rate varies extensively (characterized by the span of I in figure 7j). As such, F_{seg}^k is negligible compared to F_{seg}^g (figure 7k). This finding matches our recent results (Jing *et al.* 2020) showing that segregation forces in inclined chute flows scale primarily with pressure gradients but not shear rate gradients.

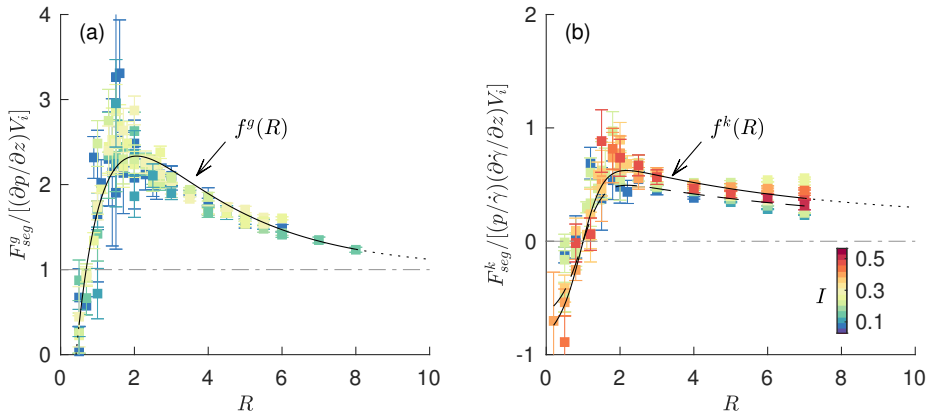


FIGURE 8. Pre-factors of (a) gravity- and (b) kinematics-related components of F_{seg} vs. R for controlled-velocity flows. Data in (a) are from Jing *et al.* (2020) where constant-shear-rate flows with gravity ($C_0 = 0$, $g = 9.81$ m/s²) are used, while simulations in (b) are constant-curvature, no-gravity flows ($C_0 h / \dot{\gamma}_0 = \pm 2$, $g = 0$). In both configurations, $\dot{\gamma}_0$ and P_0 are varied to generate a range of local inertial numbers (color bar). The solid curves in (a) and (b) are semi-empirical fits described by (3.4) and (3.5), respectively, and the dotted curves indicate unexplored ranges of R . The dashed curve in (b) is a fit based only on data with $P_0 \geq 1000$ Pa (see §3.2.2). Dash-dotted horizontal lines in (a) and (b) indicate reference values for $f^g(R)$ and $f^k(R)$, respectively, when $R = 1$ (monodisperse flow).

3.2. Variation of segregation force with R

3.2.1. Scaling based on controlled-velocity results

To this point, the fitting constants f^g and f^k in scaling law (3.3) are specific to $R = 2$. However, we previously showed (Jing *et al.* 2020) in constant-shear-rate flows ($F_{seg}^k = 0$) and free surface flows ($F_{seg}^k \approx 0$) that the scaling factor for F_{seg}^g is a function of R ; see also (1.2). To illustrate this, our data for $f^g := F_{seg}^g / [-(\partial p / \partial z) V_i]$ (Jing *et al.* 2020) are reproduced in figure 8(a) for $0.05 \leq I \leq 0.24$. With this background, we now explore F_{seg}^k for $0.2 \leq R \leq 7$ using controlled-velocity, constant-curvature flows, where gravity is turned off ($F_{seg}^g = 0$), P_0 and $\dot{\gamma}_0$ are varied for a wide range of I ($0.03 \leq I \leq 0.43$), and $C_0 h / \dot{\gamma}_0 = \pm 2$ is fixed to control the local curvature. In figure 8(b), results for $f^k := F_{seg}^k / [(p / \gamma)(\partial \dot{\gamma} / \partial z) V_i]$ plotted versus R collapse onto a master curve, despite widely varying local inertial numbers (indicated by colors). Note that the $f^k(R)$ data diverges somewhat for $R \gtrsim 4$, but with no systematic dependence on I ; this diverging behavior is discussed in §3.2.2. In general, the $f^k(R)$ curve is negative for $R < 1$, increases toward a peak at $R \approx 2$, and declines as R is further increased; its shape is similar to its gravity-related counterpart $f^g(R)$ in figure 8(a).

The forms of $f^g(R)$ and $f^k(R)$ have interesting implications in relation to the underlying physics of gravity- and kinematics-induced segregation. As we previously noted (Jing *et al.* 2020), the gravity-induced segregation force approaches Archimedes' buoyancy force in the continuum limit (i.e., $f^g(\infty) \rightarrow 1$); this force appears to be enhanced by finite-size effects and the discrete nature of particle contacts for $1 \lesssim R \lesssim 10$ but weakened by kinetics-driven percolation for $R \lesssim 1$, giving rise to the peak at $R \approx 2$.

The kinematics-induced segregation force might follow a similar geometric argument but with some unique characteristics. A key observation is that $f^k(R)$ changes sign at $R \approx 1$. Indeed, no net segregation force (perpendicular to shear) is expected for $R = 1$, which is simply a monodisperse flow. The physical implications of the negative and positive parts of $f^k(R)$ for $R < 1$ and $R > 1$, respectively, are discussed below.

Collision dominant for small intruders. For $R < 1$, $f^k(R)$ is negative, indicating that a small intruder is pushed from higher shear rate regions toward lower shear rate regions; this is reminiscent of a collisional argument in dilute granular flows whereby particles migrate from higher to lower granular temperatures (Jenkins & Yoon 2002; Trujillo *et al.* 2003; Fan & Hill 2011). Although the flows described here are dense ($I \lesssim 0.5$), contact forces acting on a *small* intruder are primarily collisional (as opposed to enduring) as a small intruder tends to percolate through voids (Silbert *et al.* 2007; Jing *et al.* 2017). As a result, small intruders experience larger contact forces from the “hotter” (higher shear rate and hence higher granular temperature) side and are thereby pushed toward the “cooler” side, corresponding to $f^k(R) < 0$ for $R < 1$.

Friction dominant for large intruders. For $R > 1$, intruder particles tend to undergo more enduring frictional contacts rather than collisional contacts (Fan & Hill 2011; Jing *et al.* 2017). Enduring contact forces are expected to be enhanced by a lower shear rate due to the increase in force correlation length, or cluster size (Lois *et al.* 2006; Fan & Hill 2011), as well as the increase in contact duration (Silbert *et al.* 2007). As a result, *large* intruders experience larger contact forces from lower shear rate regions and are thereby pushed toward higher shear rate regions, which corresponds to $f^k(R) > 0$ for $R > 1$. The peak of $f^k(R)$ at $R \approx 2$ indicates that the frictional effect is enhanced due to finite-size effects similar to those for $f^g(R)$ (Jing *et al.* 2020), which tend to diminish as $R \rightarrow \infty$ (toward the continuum limit).

$R \rightarrow \infty$ limit for $f^k(R)$. When $R \rightarrow \infty$, the flow of bed particles surrounding an intruder can be viewed as a continuum (a complex fluid), and it is intriguing to consider if the segregation force has a parallel in Newtonian fluid flows. However, unlike the Archimedian buoyancy limit for the gravity-induced segregation force, i.e., $f^g(\infty) \rightarrow 1$ (see figure 8a), the behavior of $f^k(R)$ for $R \rightarrow \infty$ is less straightforward (figure 8b). The force (perpendicular to shear and toward higher shear rates) induced by the curvature of a flow velocity profile is reminiscent of the “shear gradient lift force,” F_{SG} , for inertial focusing in microfluidics (Martel & Toner 2014), which is also known as the *tubular pinch* effect (Segré & Silberberg 1961; Matas *et al.* 2004). Despite the complex dependence of F_{SG} on the flow Reynolds number Re and the particle distance to the channel wall z/D_h , where D_h is the hydraulic diameter of the channel, a scaling law for F_{SG} has been derived for small particle Reynolds numbers (Asmolov 1999) and empirically determined in microfluidic systems (Di Carlo *et al.* 2009) as $F_{\text{SG}} = C_{\text{SG}} \rho_f U_m^2 a^3 / D_h$, where ρ_f is the fluid density, U_m is the maximum channel flow velocity, a is the particle radius (i.e., $a = d_i/2$ here), and the lift coefficient C_{SG} is a dimensionless function of Re , z/D_h , and a/D_h . Note that for channel flows of a Newtonian fluid, the velocity profile is typically parabolic (similar to our velocity profile (2.1)) with U_m appearing at the centerline and has a constant shear rate gradient $\partial\dot{\gamma}/\partial z \propto U_m/D_h^2$. For a shear rate scale U_m/D_h and a (hydrodynamic) pressure scale $\rho_f U_m^2$, we have $F_{\text{seg}}^k \propto (p/\dot{\gamma})(\partial\dot{\gamma}/\partial z)V_i^3 \propto \rho_f U_m^2 a^3 / D_h$, consistent with the scaling of F_{SG} . Therefore, it seems plausible to connect our kinematics-induced segregation force (in the large R limit) with the shear gradient lift force that is partly responsible for cross-streamline migration of particles in confined fluid flows from lower to higher shear rate regions. Of course, further investigation is warranted to shed more light on this connection as well as to consider other inertial lift forces as a possible continuum limit for F_{seg}^k , such as those induced by wall effects (Martel & Toner 2014; Ekanayake *et al.* 2020), slip velocity (Asmolov 1999; Ekanayake *et al.* 2020), and the Saffman lift effect (Saffman 1965; van der Vaart *et al.* 2018). Nevertheless, based on the understanding and scaling arguments above, we assume that $f^k(R)$ approaches a positive finite value (denoted as f_∞^k) as $R \rightarrow \infty$ and use this assumption to constrain our empirical fit in the subsequent analysis.

It is convenient to fit the collapsed data in figure 8 to functions, but it is unclear how to derive such functions analytically because they would need to bridge two unrelated physical phenomena: brief intermittent collisions at small R and enduring multiple contacts at large R . In our previous work (Jing *et al.* 2020), we use a double-exponential function to fit the data in figure 8(a) based on the understanding that the two geometric effects explained above (percolation for $R \lesssim 1$ and enhanced frictional contacts for $R \gtrsim 1$) tend to saturate as R increases, and that exponential decays are not uncommon in segregation phenomena (Savage & Lun 1988; Khola & Wassgren 2016; Schlick *et al.* 2015). The semi-empirical fit for $f^g(R)$ is

$$f^g(R) = \left[1 - c_1^g \exp\left(-\frac{R}{R_1^g}\right)\right] \left[1 + c_2^g \exp\left(-\frac{R}{R_2^g}\right)\right], \quad (3.4)$$

where $R_1^g = 0.92$, $R_2^g = 2.94$, $c_1^g = 1.43$, and $c_2^g = 3.55$ are fitting parameters (Jing *et al.* 2020). A detailed explanation for the expression (3.4), along with evidence for an exponential decay of an enhanced contact number density around the intruder as R increases, is provided by Jing *et al.* (2020). Briefly, the first term accounts for necessary percolation at small R and the second term accounts for enhanced enduring contacts acting on the intruder at large R .

Here we fit the data for $f^k(R)$ in figure 8(b) to a functional form similar to (3.4):

$$f^k(R) = f_\infty^k \left[\tanh\left(\frac{R-1}{R_1^k}\right) \right] \left[1 + c_2^k \exp\left(-\frac{R}{R_2^k}\right)\right], \quad (3.5)$$

where $f_\infty^k = 0.19$, $R_1^k = 0.59$, $R_2^k = 5.48$, and $c_2^k = 3.63$ are fitting parameters. Compared to (3.4), a non-unity pre-factor f_∞^k is used to match the assumption that $f^k(\infty) \rightarrow f_\infty^k$, and the first exponential function is replaced by a hyperbolic tangent function (i.e., $\tanh[(R-1)/R_1^k]$, which passes through zero at $R = 1$ and approaches 1 and -1 for $R \gtrsim 2$ and $R \rightarrow 0$, respectively) to better match the data for $0 < R \lesssim 2$ in figure 8(b). Although the latter modification is phenomenological, it is interesting to note that the fitted ‘‘shape factor’’ R_1^k for the tanh function in (3.5) is similar to R_1^g in the first exponential function of (3.4) in that the values are similar in magnitude and less than one. The similarity comes about because both indicate that the geometric effects related to small intruders (percolation and collision dominant for $R < 1$) decay with a ‘‘characteristic size ratio’’ of order one. Likewise, the second exponential function of (3.4) and (3.5) each decay with a ‘‘characteristic size ratio’’ (R_2^g and R_2^k , respectively) that has a physically relevant value, considering the observation that the contact number density around an intruder increases sharply with R for $R \lesssim 3$ and saturates for $R \gtrsim 5$; see Jing *et al.* (2020).

Despite the physical intuition associated with our semi-empirical models (3.4) and (3.5), one might choose other forms to fit the data in figure 8. Ideally, a theoretically grounded approach for determining $f^g(R)$ and $f^k(R)$ may be possible, perhaps one that extends kinetic theories for segregation (Jenkins & Yoon 2002; Trujillo *et al.* 2003; Duan *et al.* 2020b) into the dense limit.

3.2.2. Validation of R -scaling in other flow geometries

Although the unified scaling (1.3) is based on a wide range of flow conditions in figure 1(a-c), the dependence of the semi-empirical relations (3.4) and (3.5) on R shown in figure 8 are exclusively based on controlled-velocity confined flow conditions (figure 1a), where parameters for $f^g(R)$ and $f^k(R)$ are calibrated separately by eliminating velocity profile curvatures and gravity, respectively. To validate the R -scaling for flow geometries where gravity and flow curvatures coexist, we focus on an inclined chute flow and a

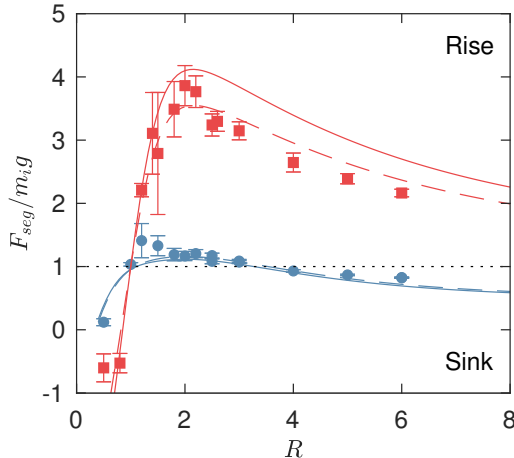


FIGURE 9. Validation of predicted $F_{seg}/m_i g$ vs. R in inclined chute flow (blue circles) ($h/d \approx 40$, $\theta = 24^\circ$, and $g = 9.81 \text{ m/s}^2$) and wall-driven flow (red squares) ($h/d \approx 40$, $P_0 = 1500 \text{ Pa}$, $\dot{\gamma}_0 = 20 \text{ s}^{-1}$, and $g = 3 \text{ m/s}^2$) with varying R . Solid curves are predictions based on the scaling law (1.3) and the empirical fitting functions (3.4) and (3.5). Dashed curves are predictions based on a refitted $f^k(R)$ curve considering only a subset of data with $P_0 \geq 1000 \text{ Pa}$ (see figure 8 and text). Model inputs for predictions are *local* flow properties at the height of the intruder $z_{eq} \approx 0.5h$ taken from corresponding simulations. Areas above and below the dotted horizontal line at $F_{seg}/m_i g = 1$ indicate where the intruder tends to rise and sink, respectively.

horizontal wall-driven confined flow, varying R in each case and comparing the predicted F_{seg} with simulation results (figure 9).

First, consider results for varying R in an inclined chute flow ($\theta = 24^\circ$, $g = 9.81 \text{ m/s}^2$) in figure 9, where local flow properties at $z = z_{eq}$ are $-\partial p/\partial z = 1.3 \times 10^4 \text{ Pa/m}$ and $(p/\dot{\gamma})(\partial \dot{\gamma}/\partial z) = -0.6 \times 10^4 \text{ Pa/m}$. The resulting kinematic term is nearly ten times smaller than the gravity term, noting that the pre-factor f^k is about one-fourth of f^g (figure 8). Calculating the appropriate pre-factors using (3.4) and (3.5) based on R and substituting them into (1.3) yields a prediction (blue solid curve in figure 9) that agrees well with simulation results (blue circles). Note that we report $F_{seg}/m_i g z$ in figure 9 to indicate whether an intruder tends to rise or sink; if $F_{seg}/m_i g z > 1$, the segregation force is greater than the intruder weight and thereby pushes the intruder upward, whereas if $F_{seg}/m_i g z < 1$, the segregation force is insufficient to support the intruder weight and the intruder sinks. For the inclined chute flow, a large intruder with $1 < R < 4$ tends to rise, while a small intruder ($R < 1$) sinks, agreeing with the tendency of “normal” segregation. However, for $R > 4$ the intruder tends to sink due to its large weight, known as “reverse” segregation (Félix & Thomas 2004).

For the second case of a wall-driven flow ($P_0 = 1500 \text{ Pa}$, $\dot{\gamma}_0 = 20 \text{ s}^{-1}$, $g = 3 \text{ m/s}^2$) with local flow properties $-\partial p/\partial z = 0.4 \times 10^4 \text{ Pa/m}$ and $(p/\dot{\gamma})(\partial \dot{\gamma}/\partial z) = 3.3 \times 10^4 \text{ Pa/m}$, the kinematics contribution is approximately two times larger than its gravity counterpart, and, importantly, both terms are positive. This leads to a much larger predicted segregation force (red solid curve), which agrees well with simulation results (red squares) for $R \lesssim 2$. However, the agreement beyond $R > 2$ is not as good. Recalling that the $f^k(R)$ data in figure 8(b) show growing scatter for $R \gtrsim 4$, the mismatch may be attributed to additional mechanisms not considered in our scaling, especially for this range of R . To understand this, we have examined the effects of the inertial number (which considers case-specific $\dot{\gamma}$ and p), stiffness of the virtual spring that is attached to the intruder, the thickness of the flowing layer, and the domain size (particularly in the

spanwise direction), but none of these explain the mismatch. One possible mechanism lies in the overburden pressure: for $P_0 \geq 1000$ Pa, $f^k(R)$ values in figure 8(b) tend to appear near the lower edge of the scatter, especially for $R > 2$, regardless of the local shear rate varying from 10 s^{-1} to 40 s^{-1} . This becomes evident when fitting (3.5) to only the data with $P_0 \geq 1000$ Pa, corresponding to the dashed curve in figure 8(b). On the other hand, all wall-driven flows we consider (including those in figure 9) fall into this higher overburden pressure category (which have $P_0 \geq 1500$ Pa) in order to ensure a flowing layer that is $10d$ to $30d$ thick (wall-driven flows tend to localize near the top wall). Hence, using the fit to (3.5) based on the subset of the $f^k(R)$ data with $P_0 \geq 1000$ Pa (dashed curve in figure 8b) significantly improves the agreement of the predicted (red dashed) curve with wall-driven data in figure 9. Although we do not have an explanation for this secondary overburden pressure dependence (which is not characterized by the inertial number and is reminiscent of nonlocal effects in granular flows), it appears to be only significant for very large intruders in shear-dominant cases. It might be plausible to examine if local velocity fluctuations (relative to local pressure) play a role (Kim & Kamrin 2020), but this is beyond the scope of this work. Note that the prediction for the inclined chute flow (blue dashed curve in figure 9) is not affected by this treatment, because the kinematics contribution associated with $f^k(R)$ is negligible in free surface flows (Jing *et al.* 2020).

Nevertheless, we stress that even without the overburden pressure-specific treatment, the overall agreement in figure 9 is still promising, especially given that the prediction for two very different flow geometries (wall-driven and free surface) is based purely on independent velocity-controlled flows, and the discrepancy is not larger than the inherent scatter of the data in figure 8. More interestingly, it is clear from figure 9 that $F_{seg}/m_i g_z$ in wall-driven flows is well above one for $R > 1$ due to the strong *positive* kinematics contribution (as predicted by our scaling law), and, as a result, the reverse segregation regime ($F_{seg}/m_i g_z < 1$) is difficult to reach by varying R alone; indeed, our model predicts that a crossover will occur at $R \approx 13$ for this wall-driven flow. The significant difference between the rise-sink transitions indicated by $F_{seg}/m_i g_z$ in inclined chute and wall-driven flows may explain why results based on confined flow simulations alone fail to predict the sinking of very large intruders as noted by Guillard *et al.* (2016), even though this behavior is observed in free surface flow experiments (Félix & Thomas 2004).

4. Conclusions

In this paper, we have used extensive DEM simulations to develop a unified description of the gravity- and kinematics-induced segregation forces on an intruder particle in dense granular flows. It is based on a fundamental scaling law (1.3) that has been validated for flows in various confined and free surface geometries. The scaling law has two additive terms, one related to gravity (buoyancy-like) and the other related to flow kinematics (specifically, the shear rate gradient); semi-empirical pre-factors for both terms depend only on the particle size ratio but not local flow properties, although the overburden pressure might cause a slight secondary effect for very large intruders. The relative significance of the two contributions vary, and this unified description of segregation forces enhances our understanding of the tendency and physical origin of segregation in different flow geometries. For free surface flows where the velocity profile typically has small shear rate gradients, the gravity-induced segregation force dominates. In fact, rising and sinking of intruders in free surface flows can be predicted by comparing the size-corrected buoyancy force alone with the intruder weight, resulting in a phase diagram determined only by the size and density ratios (Jing *et al.* 2020). For vertical

silo flows where segregation is normal to gravity, kinematics-induced segregation forces cause large (small) intruders to migrate toward (away from) the wall, consistent with previous results (Fan & Hill 2011). Both mechanisms are significant in wall-driven flows (where they cooperate) and inclined wall-driven flows (where they either cooperate or compete, depending on the angle of inclination).

The physical origin of the kinematics-induced segregation force is clarified by considering its shear rate gradient-based scaling and the nature of contact forces acting on an intruder: for large intruders ($R > 1$), which experience enduring frictional forces, larger forces are possible for lower shear rates (more persistent), whereas for small intruders ($R < 1$), which preferentially receive collisional forces, larger forces occur in higher shear rate regions (more impulsive). It is also interesting that for wall-driven flows, which are relevant to annular shear (Golick & Daniels 2009) and fluid-driven bedload transport (Ferdowsi *et al.* 2017), both segregation-driving mechanisms (gravity- and kinematics-induced) act in the same direction against gravity and, therefore, sinking of large particles due to weight effects does not occur as readily as in free surface flows (Félix & Thomas 2004). From a practical standpoint, our results suggest that it may be possible to design experimental or industrial devices that minimize segregation (or, equivalently, enhance particle mixing) by manipulating the velocity profile (e.g., inclined wall-driven flows with appropriate inclinations), such that the kinematics-induced contribution to the segregation force counteracts gravitational contributions.

The unified description of segregation forces presented here is based on the limit where the intruder concentration approaches zero. However, the question naturally arises as to its applicability at higher intruder concentrations. We have already demonstrated (Jing *et al.* 2020) that it compares well with free surface flow experiments (Félix & Thomas 2004) for larger concentrations (about 10%) where intruder particles interact with each other infrequently and gravity-induced segregation forces dominate over kinematics-induced forces. Recent work also indicates that under certain conditions combined size and density segregation can be nearly independent of either the particle size or density ratio at small concentrations, but further increasing the concentration leads to significant changes in the segregation behavior (Duan *et al.* 2020a). Understanding how segregation forces depend on the particle concentration is of great interest due to the complex concentration dependence of segregation fluxes (Gajjar & Gray 2014; van der Vaart *et al.* 2015; Gray & Ancey 2015; Jing *et al.* 2017; Jones *et al.* 2018; Duan *et al.* 2020a). Extending the current model toward finite intruder particle concentrations has the potential to further elucidate the underlying physics of granular segregation as well as to enhance continuum modeling of granular segregation, which will be addressed in future work.

Finally, the segregation force studied in this paper, as well as in Guillard *et al.* (2016), van der Vaart *et al.* (2018), and Jing *et al.* (2020), is measured on intruder particles tethered to a virtual spring, which effectively prevents segregation. That is, the *mean* relative velocity between the intruder and bed particles is zero in the segregation (z) direction once the intruder reaches an equilibrium z -position. If the intruder is *untethered* and the net force is unbalanced, a relative velocity between the intruder and its surrounding bed particles will develop (Tripathi & Khakhar 2011; Staron 2018), leading to a resistive force (often viewed as the drag force) that can be associated with the relative velocity as well as other parameters. Previous studies on the drag force during particle segregation have focused on density-bidisperse but size-monodisperse flows (Tripathi & Khakhar 2011; Duan *et al.* 2020b) due to the lack of a general description of the segregation force. With the segregation force model developed here, it is now possible to

study the drag force in more general segregation situations where particles differ in both size and density.

Acknowledgements

We thank Yi Fan, John Hecht, and Yifei Duan for valuable discussions. This material is based upon work supported by the National Science Foundation under Grant No. CBET-1929265, and was facilitated in part by the computational resources and staff contributions provided by the Quest high performance computing facility at Northwestern University, which is jointly supported by the Office of the Provost, the Office for Research, and Northwestern University Information Technology.

Appendix A. Connection with a previous model

Here we demonstrate how our $\partial\dot{\gamma}/\partial z$ -based scaling (1.3) is connected with the previous scaling (1.1) where $\partial\tau/\partial z$ is used (Guillard *et al.* 2016) when a local rheology is assumed. For simplicity, we adopt a linear rheological law,

$$\mu(I) = \mu_s + bI, \quad (\text{A } 1)$$

where μ_s and b are constants. The linear form (da Cruz *et al.* 2005) is a good approximation of our $\mu(I)$ data, at least for $I < 0.3$ (see figure 6).

Expressing $\partial\tau/\partial z$ using (A 1) with $\tau = \mu p$ and $I = \dot{\gamma}d/\sqrt{p/\rho}$, we have

$$\frac{\partial\tau}{\partial z} = \mu \frac{\partial p}{\partial z} + p \frac{\partial\mu}{\partial z} = \mu \frac{\partial p}{\partial z} + p \frac{\partial}{\partial z} \left(b \frac{\dot{\gamma}d}{\sqrt{p/\rho}} \right). \quad (\text{A } 2)$$

Expanding (A 2) and eliminating b by identifying $b = (\mu - \mu_s)/I$ yields

$$\frac{\partial\tau}{\partial z} = \frac{1}{2}(\mu + \mu_s) \frac{\partial p}{\partial z} + (\mu - \mu_s) \frac{p}{\dot{\gamma}} \frac{\partial\dot{\gamma}}{\partial z}. \quad (\text{A } 3)$$

Rearranging and substituting (A 3) into (1.3), we have

$$F_{seg} = - \underbrace{\left[f^g(R) + \frac{1}{2} f^k(R) \frac{\mu + \mu_s}{\mu - \mu_s} \right]}_{\sim \mathcal{A}(\mu, R)} \frac{\partial p}{\partial z} V_i + \underbrace{\frac{f^k(R)}{\mu - \mu_s}}_{\sim \mathcal{B}(\mu, R)} \frac{\partial\tau}{\partial z} V_i, \quad (\text{A } 4)$$

where $f^g(R)$ and $f^k(R)$ are pre-factors of our scaling (1.3), while the under-braced terms are rational functions of μ with shapes similar to $\mathcal{A}(\mu, R)$ and $\mathcal{B}(\mu, R)$ in (1.1), which are described by exponential functions in Guillard *et al.* (2016).

From this analysis, it is clear that the μ dependence in (1.1) emerges as a result of the adopted $\mu(I)$ rheology that connects τ and $\dot{\gamma}$ via a unique function. Although our kinematics-based scaling (1.3) can be transformed into the stress-based scaling (1.1) with certain assumptions, we note that our scaling decouples gravity- and shear-induced (or kinematics-induced) segregation forces. Consequently, each of the resulting terms requires fewer fitting parameters (insensitive to μ). It also seems to be more general across flow geometries where $\mu(I)$ might not follow a unique function, which is often the case for confined flows or near the edge of flowing regions. Finally, the shear-rate-gradient-based scaling helps reveal important aspects of the underlying physics of kinematics-induced segregation in dense granular flows.

REFERENCES

- ASMOLOV, E. S. 1999 The inertial lift on a spherical particle in a plane Poiseuille flow at large channel Reynolds number. *J. Fluid Mech.* **381**, 63–87.
- CHASSAGNE, R., MAURIN, R., CHAUCHAT, J., GRAY, J. M. N. T. & FREY, P. 2020 Discrete and continuum modelling of grain size segregation during bedload transport. *J. Fluid Mech.* **895**, A30.
- CLARK, A. H., THOMPSON, J. D., SHATTUCK, M. D., OUELLETTE, N. T. & O’HERN, C. S. 2018 Critical scaling near the yielding transition in granular media. *Phys. Rev. E* **97** (6), 062901.
- DA CRUZ, F., EMAM, S., PROCHNOW, M., ROUX, J. & CHEVOIR, F. 2005 Rheophysics of dense granular materials: discrete simulation of plane shear flows. *Phys. Rev. E* **72**, 021309.
- DI CARLO, D., EDD, J. F., HUMPHRY, K. J., STONE, H. A. & TONER, M. 2009 Particle segregation and dynamics in confined flows. *Phys. Rev. Lett.* **102** (9), 094503.
- DUAN, Y., UMBANHOWAR, P. B., OTTINO, J. M. & LUEPTOW, R. M. 2020a Modelling segregation of flowing bidisperse granular mixtures varying simultaneously in size and density. *arXiv:2011.09018 [cond-mat]* .
- DUAN, Y., UMBANHOWAR, P. B., OTTINO, J. M. & LUEPTOW, R. M. 2020b Segregation models for density-bidisperse granular flows. *Phys. Rev. Fluids* **5** (4), 044301.
- EKANAYAKE, N. I. K., BERRY, J. D., STICKLAND, A. D., DUNSTAN, D. E., MUIR, I. L., DOWER, S. K. & HARVIE, D. J. E. 2020 Lift and drag forces acting on a particle moving with zero slip in a linear shear flow near a wall. *J. Fluid Mech.* **904**, A6.
- FAN, Y. & HILL, K. M. 2011 Phase transitions in shear-induced segregation of granular materials. *Phys. Rev. Lett.* **106** (21), 218301.
- FAN, Y., SCHLICK, C. P., UMBANHOWAR, P. B., OTTINO, J. M. & LUEPTOW, R. M. 2014 Modelling size segregation of granular materials: the roles of segregation, advection and diffusion. *J. Fluid Mech.* **741**, 252–279.
- FÉLIX, G. & THOMAS, N. 2004 Evidence of two effects in the size segregation process in dry granular media. *Phys. Rev. E* **70** (5), 051307.
- FERDOWSI, B., ORTIZ, C. P., HOUSSAIS, M. & JEROLMACK, D. J. 2017 River-bed armouring as a granular segregation phenomenon. *Nat. Commun.* **8** (1), 1363.
- FORTERRE, Y. & POULIQUEN, O. 2008 Flows of Dense Granular Media. *Annu. Rev. Fluid Mech.* **40** (1), 1–24.
- FREY, P. & CHURCH, M. 2009 How river beds move. *Science* **325** (5947), 1509–1510.
- FRY, A. M., UMBANHOWAR, P. B., OTTINO, J. M. & LUEPTOW, R. M. 2018 Effect of pressure on segregation in granular shear flows. *Phys. Rev. E* **97** (6), 062906.
- GAJJAR, P. & GRAY, J. M. N. T. 2014 Asymmetric flux models for particle-size segregation in granular avalanches. *J. Fluid Mech.* **757**, 297–329.
- GDR MiDi 2004 On dense granular flows. *The European Physical Journal E* **14** (4), 341–365.
- GOLICK, L. A. & DANIELS, K. E. 2009 Mixing and segregation rates in sheared granular materials. *Phys. Rev. E* **80** (4), 042301.
- GRAY, J. M. N. T. 2018 Particle segregation in dense granular flows. *Annu. Rev. Fluid Mech.* **50** (1), 407–433.
- GRAY, J. M. N. T. & ANCEY, C. 2015 Particle-size and -density segregation in granular free-surface flows. *J. Fluid Mech.* **779**, 622–668.
- GRAY, J. M. N. T. & THORNTON, A. R. 2005 A theory for particle size segregation in shallow granular free-surface flows. *Proc. R. Soc. A.* **461** (2057), 1447–1473.
- GUILLARD, F., FORTERRE, Y. & POULIQUEN, O. 2016 Scaling laws for segregation forces in dense sheared granular flows. *J. Fluid Mech.* **807**, R1.
- HILL, K. M. & TAN, D. S. 2014 Segregation in dense sheared flows: gravity, temperature gradients, and stress partitioning. *J. Fluid Mech.* **756**, 54–88.
- ITOH, R. & HATANO, T. 2019 Geological implication of grain-size segregation in dense granular matter. *Philos. T. R. Soc. A* **377** (2136), 20170390.
- IVERSON, R. M. 1997 The physics of debris flows. *Rev. Geophys.* **35** (3), 245–296.
- JENKINS, J. T. & YOON, D. K. 2002 Segregation in binary mixtures under gravity. *Phys. Rev. Lett.* **88** (19), 194301.

- JING, L., KWOK, C. Y. & LEUNG, Y. F. 2017 Micromechanical origin of particle size segregation. *Phys. Rev. Lett.* **118** (11), 118001.
- JING, L., KWOK, C. Y., LEUNG, Y. F. & SOBRAL, Y. D. 2016 Characterization of base roughness for granular chute flows. *Phys. Rev. E* **94** (5), 052901.
- JING, L., OTTINO, J. M., LUEPTOW, R. M. & UMBANHOWAR, P. B. 2020 Rising and sinking intruders in dense granular flows. *Phys. Rev. Res.* **2** (2), 022069.
- JOHNSON, C. G., KOKELAAR, B. P., IVERSON, R. M., LOGAN, M., LAHUSEN, R. G. & GRAY, J. M. N. T. 2012 Grain-size segregation and levee formation in geophysical mass flows. *J. Geophys. Res.* **117** (F1), F01032.
- JONES, R. P., ISNER, A. B., XIAO, H., OTTINO, J. M., UMBANHOWAR, P. B. & LUEPTOW, R. M. 2018 Asymmetric concentration dependence of segregation fluxes in granular flows. *Phys. Rev. Fluids* **3** (9), 094304.
- KAMRIN, K. 2019 Non-locality in granular flow: Phenomenology and modeling approaches. *Front. Phys.* **7**, 116.
- KAMRIN, K. & HENANN, D. L. 2015 Nonlocal modeling of granular flows down inclines. *Soft Matter* **11** (1), 179–185.
- KAMRIN, K. & KOVAL, G. 2012 Nonlocal constitutive relation for steady granular flow. *Phys. Rev. Lett.* **108** (17), 178301.
- KHOLA, N. & WASSGREN, C. 2016 Correlations for shear-induced percolation segregation in granular shear flows. *Powder Technol.* **288**, 441–452.
- KIM, S. & KAMRIN, K. 2020 Power-law scaling in granular rheology across flow geometries. *Phys. Rev. Lett.* **125** (8), 088002.
- KLOSS, C., GONIVA, C., HAGER, A., AMBERGER, S. & PIRKER, S. 2012 Models, algorithms and validation for opensource DEM and CFD-DEM. *Prog. Comput. Fluid Dy.* **12** (2), 140–152.
- KUMAR, A., KHAKHAR, D. V. & TRIPATHI, A. 2019 Theoretical calculation of the buoyancy force on a particle in flowing granular mixtures. *Phys. Rev. E* **100** (4), 042909.
- LARCHER, M. & JENKINS, J. T. 2015 The evolution of segregation in dense inclined flows of binary mixtures of spheres. *J. Fluid Mech.* **782**, 405–429.
- LENER, E., DÜRING, G. & WYART, M. 2012 A unified framework for non-Brownian suspension flows and soft amorphous solids. *Proc. Natl. Acad. Sci. U.S.A.* **109** (13), 4798–4803.
- LOIS, G., LEMAÎTRE, A. & CARLSON, J. M. 2006 Emergence of multi-contact interactions in contact dynamics simulations of granular shear flows. *Europhys. Lett.* **76** (2), 318.
- LOUGE, M. Y. 2003 Model for dense granular flows down bumpy inclines. *Phys. Rev. E* **67** (6).
- MARCS, B., ROGNON, P. & EINAV, I. 2012 Grainsize dynamics of polydisperse granular segregation down inclined planes. *J. Fluid Mech.* **690**, 499–511.
- MARTEL, J. M. & TONER, M. 2014 Inertial focusing in microfluidics. *Annu. Rev. Biomed. Eng.* **16** (1), 371–396.
- MATAS, J.-P., MORRIS, J. F. & GUAZZELLI, É. 2004 Inertial migration of rigid spherical particles in Poiseuille flow. *J. Fluid Mech.* **515**, 171–195.
- OTTINO, J. M. & KHAKHAR, D. V. 2000 Mixing and Segregation of Granular Materials. *Annu. Rev. Fluid Mech.* **32** (1), 55.
- OTTINO, J. M. & LUEPTOW, R. M. 2008 On mixing and demixing. *Science* **319** (5865), 912–913.
- SAFFMAN, P. G. 1965 The lift on a small sphere in a slow shear flow. *J. Fluid Mech.* **22** (2), 385–400.
- SAITOH, K. & TIGHE, B. P. 2019 Nonlocal effects in inhomogeneous flows of soft athermal disks. *Phys. Rev. Lett.* **122** (18), 188001.
- SAVAGE, S. B. & LUN, C. K. K. 1988 Particle size segregation in inclined chute flow of dry cohesionless granular solids. *J. Fluid Mech.* **189**, 311–335.
- SCHLICK, C. P., FAN, Y., ISNER, A. B., UMBANHOWAR, P. B., OTTINO, J. M. & LUEPTOW, R. M. 2015 Modeling segregation of bidisperse granular materials using physical control parameters in the quasi-2d bounded heap. *AIChE J.* **61** (5), 1524–1534.
- SEGRÉ, G. & SILBERBERG, A. 1961 Radial particle displacements in Poiseuille flow of suspensions. *Nature* **189** (4760), 209–210.
- SILBERT, L. E., ERTAŞ, D., GREST, G. S., HALSEY, T. C., LEVINE, D. & PLIMPTON, S. J. 2001 Granular flow down an inclined plane: Bagnold scaling and rheology. *Phys. Rev. E* **64** (5), 051302.

- SILBERT, L. E., GREY, G. S., BREWSTER, R. & LEVINE, A. J. 2007 Rheology and contact lifetimes in dense granular flows. *Phys. Rev. Lett.* **99** (6), 068002.
- SILBERT, L. E., LANDRY, J. W. & GREY, G. S. 2003 Granular flow down a rough inclined plane: Transition between thin and thick piles. *Phys. Fluids* **15** (1), 1.
- STARON, L. 2018 Rising dynamics and lift effect in dense segregating granular flows. *Phys. Fluids* **30** (12), 123303.
- THOMAS, N. 2000 Reverse and intermediate segregation of large beads in dry granular media. *Phys. Rev. E* **62** (1), 961–974.
- TRIPATHI, A. & KHAKHAR, D. V. 2011 Numerical simulation of the sedimentation of a sphere in a sheared granular fluid: A granular Stokes experiment. *Phys. Rev. Lett.* **107** (10), 108001.
- TRUJILLO, L., ALAM, M. & HERRMANN, H. J. 2003 Segregation in a fluidized binary granular mixture: Competition between buoyancy and geometric forces. *Europhys. Lett.* **64** (2), 190–196.
- TUNUGUNTLA, D. R., WEINHART, T. & THORNTON, A. R. 2016 Comparing and contrasting size-based particle segregation models. *Comput. Part. Mech.* **4** (4), 1–19.
- UMBANHOWAR, P. B., LUEPTOW, R. M. & OTTINO, J. M. 2019 Modeling segregation in granular flows. *Annu. Rev. Chem. Biomol. Eng.* **10** (1), 5.1–5.25.
- VAN DER VAART, K., GAJJAR, P., EPELY-CHAUVIN, G., ANDREINI, N., GRAY, J. M. N. T. & ANCEY, C. 2015 Underlying asymmetry within particle size segregation. *Phys. Rev. Lett.* **114** (23), 238001.
- VAN DER VAART, K., VAN SCHROJENSTEIN LANTMAN, M. P., WEINHART, T., LUDING, S., ANCEY, C. & THORNTON, A. R. 2018 Segregation of large particles in dense granular flows suggests a granular Saffman effect. *Phys. Rev. Fluids* **3** (7), 074303.
- WEINHART, T., THORNTON, A. R., LUDING, S. & BOKHOVE, O. 2012 Closure relations for shallow granular flows from particle simulations. *Granul. Matter* **14** (4), 531–552.
- ZHANG, N. F. 2006 Calculation of the uncertainty of the mean of autocorrelated measurements. *Metrologia* **43** (4), S276–S281.